PCCP

Accepted Manuscript

ROYAL SOCIETY OF CHEMISTRY

www.rsc.org/pccp

Phys. Chem. Chem. Phys RSC Publishing

PAPER

Mechanism of visible light photocatalytic NOx oxidation with plasmonic Bi cocatalyst-enhanced $(BiO)_2CO_3$ hierarchical microspheres

Received (in XXX, XXX) Xth XXXXXXXXX 20XX,

Accepted Xth XXXXXXXXX 20XX

Yanjuan Sun [a],* Zaiwang Zhao [a], Fan Dong [a], Wei Zhang [b],*

[a] *College of Environmental and Biological Engineering, Chongqing Key Laboratory of Catalysis and Functional Organic Molecules, Chongqing Technology and Business University, Chongqing 400067, China.*

[b] *Chongqing Institute of Green and Intelligent Technology, Chinese Academy of Sciences, Chongqing 400714, China.*

DOI: 10.1039/b000000x

Semimetal bismuth (Bi), as an emerging non-noble metal-based cocatalyst and plasmonic photocatalyst, has attracted significant attention. In this work, one-pot solvent-controlled synthesis strategy was firstly utilized to in situ-deposit plasmonic Bi nanoparticles onto the surface of $(BiO)_2CO_3$ microspheres (BOC-WE) using bismuth citrate, sodium carbonate, and ethylene glycol as precursors. The introduction of Bi nanoparticles have pivotal effects on the morphology, optical and photocatalytic performance of pristine $(BiO)_2CO_3$. The results indicated that the Bi nanoparticles were generated on the surface of $(BiO)_2CO_3$ microspheres via the in situ reduction of Bi^{3+} by ethylene glycol. The Bi-deposited $(BiO)_2CO_3$ microspheres were applied for photocatalytic purification of NOx in air under visible light irradiation. Significantly, the BOC-WE samples exhibited a drastically promoted photocatalytic performance with a NOx removal ratio (η) of 37.2%, superior to pristine $(BiO)_2CO_3$ (η=19.1%), and outperforms that of other well-known visible light photocatalysts, such as C-doped TiO_2 (η=21.8%), BiOBr (η=21.3%), BiOI (η=14.9%) and C_3N_4 (η=25.5%). The conspicuously enhanced photocatalytic capability can be attributed to the synergistic effects of surface plasmon resonance (SPR) effect, increased visible light absorption and efficient separation of electron–hole pairs induced by the Bi nanoparticles. The Bi nanoparticles could exert as a non-noble metal-based cocatalyst for strengthening photocatalytic performance, which is similar to the behavior of noble metals (Au, Ag) in enhancing photocatalysis. The mechanism of visible light photocatalytic NOx oxidation was investigated. DMPO-ESR spin-trapping results demonstrated that the hydroxyl radicals were confirmed to be the main active species for NOx photo-oxidation. Due to the SPR effect of Bi, the BOC-WE could produce more hydroxyl radicals than that of BOC, which was responsible for the enhanced NO photo-oxidation ability. Moreover, the BOC-WE photocatalysts showed a high photochemical stability under repeated irradiations. This work demonstrated the feasibility for the utilization of low cost Bi cocatalyst as a substitute for noble metals to enhance the performance of other photocatalysts. This work could not only provide new insights into the in situ fabrication of Bi/semiconductor nanocomposites, but also pave a new way for the modification of photocatalysts with non-noble metals as cocatalyst to achieve an enhanced performance for environmental and energetic applications.

1. Introduction

Nitrogen monoxide and dioxide (NOx), mainly produced from combustion of fossil fuels and vehicle exhaust, are regarded as typical pollutants in air, since they are responsible for atmospheric environmental problems such as haze, acid rain, and photochemical smog.[1] Although traditional techniques such as selected cataletic reduction (SCR), adsorption, biofiltration, and thermal catalysis methods could purify NOx from industrial emissions, they are not economically feasible for the removal of NOx at parts per billion (ppb) level in common indoor and outdoor atmosphere.[2] Photocatalysis, as a "green" technology, has been widely used to remove NOx at ppb level in mild conditions.[3-8]

The wide band gap of TiO_2 photocatalyst (3.2 eV) could utilize little visible light (400 nm < λ< 700 nm), which accounts for 43% of the solar energy.[2,9] With the purpose of better utilizing the solar light, modification of photocatalysts with wide gap and development of new photocatalysts with narrow band gap are highly desirable.[10-11] Recently, Bi-based photocatalysts (e.g. Bi_2WO_6, $BiVO_4$, BiOI, $Bi_4Ti_3O_{12}$ and $BiOIO_3$), have been extensively investigated owing to their relatively high photocatalytic capability.[12-16] All these Bi-based oxides belong to the layered or Aurivillius-related oxide family, whose structures are characterized by the alternative stacking of $(Bi_2O_2)^{2+}$ layers and slabs of other inorganic atoms or groups. In particular, as another lamellar compound, $(BiO)_2CO_3$ has a crystal structure of $(Bi_2O_2)_2^{+}$ layers interleaved by slabs consisting CO_3^{2-} groups, and has demonstrated potential photocatalytic applications.[16] Nevertheless, pure $(BiO)_2CO_3$ (Eg ≈ 3.3eV) suffers from shortcomings such as low visible light utilization efficiency and rapid recombination of photo-generated electron-hole pairs.[17]

Consequently, many approaches have been utilized to strengthen the visible-light photocatalytic performance of $(BiO)_2CO_3$-based photocatalysts, such as morphology modulation,[18,19] nonmetal doping,[8] noble metal deposition,[20,21] formation of heterostructures and so on.[17,22-25] Among these strategies, construction of heterostructures has demonstrated great potential to enhance the photocatalytic performance of $(BiO)_2CO_3$ as the charge carriers could transfer across the interface of the heterostructure to restrain the electron-hole pairs recombination.[22-25] For instance, Yu and co-workers reported on grapheme/$(BiO)_2CO_3$ and $BiVO_4$/$(BiO)_2CO_3$ heterostructures with elevated visible-light photocatalytic activity.[22,23] Fan and his group obtained BiOCl/$Bi_2O_2CO_3$ nanosheets with better photocatalytic performance than pristine BiOCl and $Bi_2O_2CO_3$ for MO degradation[24]. Zhang et al. prepared the sesame-biscuit-like $Bi_2O_2CO_3$/Bi_2MoO_6 nanocomposites via a facile anion exchange approach.[17] Furthermore, the $Bi_2O_2CO_3$/Bi_2S_3 heterojunctions with superior visible light photocatalytic property for RhB removal have been obtained.[25] Noble metal/$(BiO)_2CO_3$-based plasmonic photocatalysts have also been reported. Peng and Dong et al. have successfully loaded Ag nanoparticles on the $(BiO)_2CO_3$ microspheres for enhanced visible light photocatalysis.[20,21] On one hand, through surface scattering and reflecting effects (SSR effect), 3D hierarchical architectures could make pure $(BiO)_2CO_3$ visible-light-active.[21] On the other hand, surface plasmon resonance effects (SPR effect) of noble metal decorated on $(BiO)_2CO_3$ surface could further strengthen the visible light absorption of 3D $(BiO)_2CO_3$ hierarchical microspheres.[20,21]

Very recently, semimetal bismuth is found to possess direct plasmonic photocatalytic ability.[26] Similar to noble metal elements (such as Au, Ag), Bi was also an excellent noble-metal free candidate to decorate the photocatalysts with wide band gap for enhanced photocatalysis.[27-33] Especially, among these cases, Bi/$(BiO)_2CO_3$ nanocomposites exhibited extremely high photocatalytic performance as well as stability in comparation with their separate components.[33] Although Bi-deposited $(BiO)_2CO_3$ has been reported, the solvent-controlled synthesis of Bi-deposited $(BiO)_2CO_3$ has not been reported. Furthermore, the mechanism of visible light photocatalytic NOx oxidation with Bi-deposited $(BiO)_2CO_3$ is not clear and needs a detailed investigation.

In this study, we firstly developed a one-pot solvent-controlled synthesis strategy to in-situ deposit Bi cocatalyst on the surface of $(BiO)_2CO_3$ microspheres. During the solvent-controlled reaction, ethylene glycol functioned as a reductant and reduce Bi^{3+} to metallic Bi. The obtained Bi/$(BiO)_2CO_3$ microspheres demonstrated an enhanced visible-light photocatalytic capability which was much higher than that of individual $(BiO)_2CO_3$ owing to the SPR effect, enhance visible light absorption, and efficiently accelerated the electron–hole pairs separation induced by Bi nanoparticles. The catalytic behavior of Bi nanoparticles in photocatalysis as a cocatalyst is similar to that of noble metals, which demonstrated the feasibility for using low cost Bi nanoparticles as a substitute for noble metals to improve the performance of other photocatalysts. Last but truly pivotal, the as-prepared Bi/$(BiO)_2CO_3$ composites also exerted decent photochemical stability, which will pave a new way for the practical application of the Bi-based photocatalysts.

2. Experimental section

2.1 Synthesis

All the reagents employed in this study were of analytical grade and used without further purification. In a typical synthesis process, sodium carbonate (0.46 g) was first dissolved in distilled water (25 ml) in a 100 ml autoclaved Teflon vessel and then stirred for 10 min. An appropriate volume of ethylene glycol (45 ml) was then added, and the resulting solution was further stirred for 10 min. Afterward, bismuth citrate (1.6 g) was added to the solution, and the mixture was stirred for 30 min to ensure the complete dissolution of all the reagents. The resulting precursor suspension was hydrothermally treated at 160 ^{o}C for 24 h. After being cooled down to room temperature, the resulted solid was filtered, washed with water three times and ethanol once, and dried at 60 ^{o}C for 12 h to obtain the final Bi-deposited $(BiO)_2CO_3$, which was labeled as BOC-WE. Pure $(BiO)_2CO_3$ hierarchical microspheres was prepared without using ethylene glycol and labeled as BOC.[34]

2.2 Characterization

The X-ray diffraction (XRD) patterns of the samples were obtained using an X-ray diffractometer equipped with intense Cu Kα radiation (Model D/max RA, Rigaku Co., Japan). The morphological structure was analyzed using scanning electron microscope (SEM, JEOL model JSM-6490, Japan), transmission electron microscope (TEM, JEM-2010, Japan), and high-resolution transmission electron microscope (HRTEM). The Brunauer–Emmett–Teller (BET) specific surface area (S_{BET}) of the samples were determined using a nitrogen adsorption apparatus (ASAP 2020, USA) with all samples degassed at 100 °C for 12 h prior to measurements. X-ray photoelectron spectroscopy (XPS) measurement was carried out to investigate the surface chemical compositions and states with Al Kα X-ray (hv = 1486.6 eV) radiation source operated at 150 W (Thermo ESCALAB 250, USA). The UV-vis diffuse reflection spectra (UV-vis DRS) were obtained for the dry-pressed disk samples by using a Scan UV-vis spectrophotometer (UV-2450, Shimadzu, Japan) with 100% $BaSO_4$ as the standard sample. Photoluminescence (PL, F-7000, HITACHI, Japan) was used to investigate the optical properties of the obtained samples. The sample for ESR measurement (FLsp920, England) was prepared by mixing the as-prepared samples in a 50 mM DMPO (5, 5'-dimethyl-1-pirrolin e-N-oxide) solution with aqueous dispersion for DMPO-•OH. The visible light irradiation source was a 300 W Xe arc lamp (PLS-SXE 300, Beijing) system equipped with a UV cut-off filter (λ>420 nm).

2.3 Evaluation of photocatalytic activity

The photocatalytic activity of the as-synthesized samples was evaluated by removing NO at ppb level in a continuous flow reactor. The reactor was 4.5 L (30 cm × 15 cm × 10 cm), made of polymeric glass, and covered with Saint-Glass. A commercial tungsten halogen lamp (100 W) was vertically placed 20 cm above the reactor. A UV cut-off filter (420 nm) was applied to remove UV light for the test of visible light photocatalytic activity. The as-prepared sample (0.20 g) was dispersed in distilled water (50 ml) in a beaker via ultrasonic treatment for 10 min and then coated onto two glass dishes (12.0 cm in diameter). The coated dishes were pretreated at 70 °C to remove water in the suspension and were placed at the center of the reactor after cooling down to room temperature. The NO gas was acquired from a compressed gas cylinder at a concentration of 100 ppm of NO (N_2 balance). The initial concentration of NO was diluted to about 600 ppb via air streaming. The flow rates of the air stream and NO were controlled at 2.4 L min^{-1} and 15 mL min^{-1}, respectively. The two gas streams were then premixed in a three-way valve. The relative humidity was controlled at 50% in the air stream. When the adsorption-desorption equilibrium was achieved, the lamp was turned on. The concentration of NO was

measured every 1 min by using an NO_x analyzer (Thermo Scientific, 42i-TL), which also monitored the concentration of NO_2 and NO_x (NO_x represents NO + NO_2). The removal ratio (η) of NO was calculated using η (%) = $(1 - C/C_0) \times 100\%$, where C is the outlet concentration of NO after reaction for time t, and C_0 represents the inlet concentration after achieving adsorption-desorption equilibrium.

3. Results and discussion

3.1 Phase structure

The crystalline structures of the as-prepared samples are characterized by powder X-ray diffraction. Fig. 1 shows the XRD patterns of the as-prepared BOC-WE and pure BOC samples. As shown in Fig. 1a, all the diffraction peaks in agreement with the typical tetragonal $Bi_2O_2CO_3$ data (JCPDS card No. 41-1488) can be detected, demonstrated that the existence of $Bi_2O_2CO_3$. The intensity of diffraction peaks increased with the addition of ethylene glycol, which suggests that the addition of ethylene glycol results in improved crystallinity of the samples. In addition, as shown in the enlarged view of XRD (Fig. 1b), the typical (012) peak around 27.1° indexed to the rhombohedral phase of elemental Bi (JCPDS card no. 05-0519) was observed for BOC-WE sample, indicating that Bi was successfully deposited on $(BiO)_2CO_3$. No other impurity peaks can be detected which indicated that Bi-deposited $(BiO)_2CO_3$ composites have been successfully fabricated. The changes of diffraction peaks as well as lattice parameters of $(BiO)_2CO_3$ in the BOC-WE samples are also not detectable, which implies that Bi did not enter the lattice of $(BiO)_2CO_3$ but only on the surface.[20] Based on the crystal structure of $(BiO)_2CO_3$, the $(Bi_2O_2)^{2+}$ and CO_3^{2-} layers are orthogonally connected. This internal layered structure would mediate a lower growth rate along a particular axis to form morphology of nanosheet.[35]

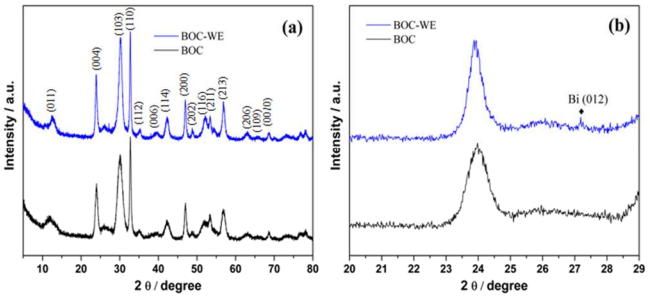

Fig. 1 XRD (a) and enlarged view (b) of BOC-WE and BOC.

3.2 Chemical composition.

To investigate the chemical composition and chemical bonding of the nanocomposites, FT-IR was carried out and the corresponding spectra are shown in Fig. 2. For pure BOC and BOC-WE, the broad peaks centered at 3445 cm^{-1} are associated with the stretching and deformation vibration of the hydroxyl function groups (O–H).[32] The presence of the sharp and strong absorption peaks at 1560 cm^{-1} can be ascribed to the bending vibration absorption of free water molecules.[36] A band corresponding to vibration of the Bi–O bond (548 cm^{-1}) was observed.[37,38] Other peaks can be indexed to symmetric stretching mode ν_1, antisymmetric vibration ν_3, the out-of-plane bending mode ν_2 and the in-plane deformation ν_4 of carbonate ions.[5]

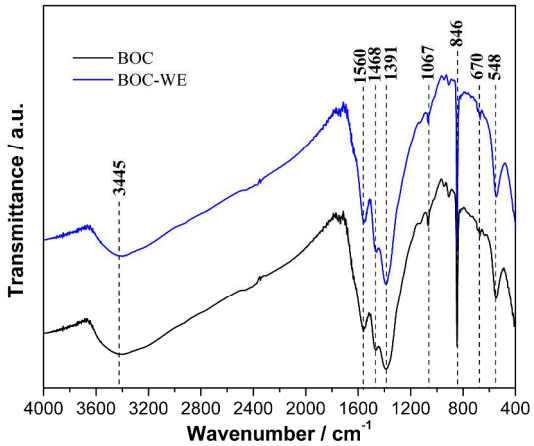

Fig. 2 FT-IR spectra of the pure BOC and BOC-WE.

XPS was further conducted to investigate the surface chemical composition of the BOC-WE sample (Fig. 3). Figure 3a shows the survey of the samples, indicating all the samples consist of Bi, O and C. The high-resolution XPS spectra for Bi4f are shown in Fig. 3b. The two strong peaks at 159.2 and 164.5 eV are ascribed to $Bi4f_{7/2}$ and $Bi4f_{5/2}$, respectively, which are the features of Bi^{3+} in $(BiO)_2CO_3$.[39] Besides, two low peaks located at 156.7 and 162.1 eV can be observed, which can be attributed to the features of metallic Bi, consistent with XRD result (Fig. 1a).[40] The concentration of Bi on the surface of Bi/BOC samples is determined to be 0.95 %. The generation of Bi elements on the surface of BOC could provide a decent explanation for the color change from white for BOC to dark gray for BOC-WE. The O1s spectra can be fitted by three peaks at binding energies of 529.6, 530.8, and 532.0 eV, respectively, which are also recorded in Figure 3c. The peak at 529.6 eV is characteristic of Bi-O binding energy in $(BiO)_2CO_3$,[41] and the other two peaks at 530.8 and 532.0 eV can be assigned to carbonate species and adsorbed H_2O (or surface hydroxyl groups) on the surface. Fig. 3d shows the C1s XPS spectra. The peaks at 284.8 is assigned to the adventitious carbon species, whereas the peak observed at 288.8 eV is ascribed to CO_3^{-2} in $(BiO)_2CO_3$. [42]

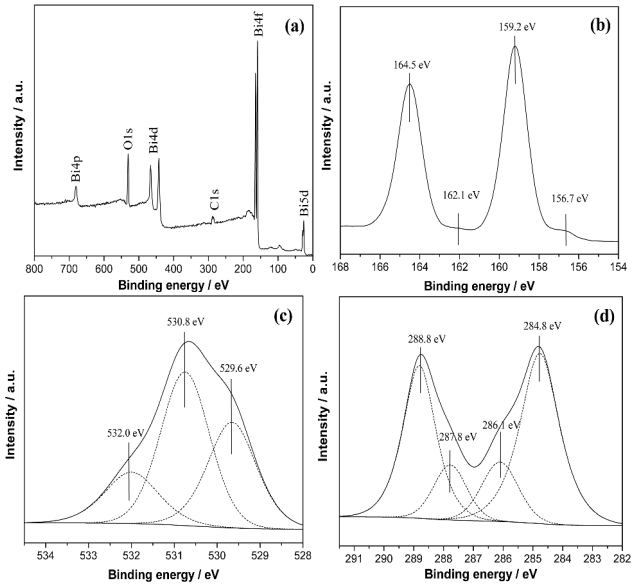

Fig. 3 XPS spectra of BOC-WE, survey (a), Bi4f (b), O1s (c) and C1s (d).

3.3 Morphological architectures

The morphology of the pure BOC and BOC-WE were characterized via SEM, TEM, and HRTEM as shown in Fig. 4 and 5, respectively. The pure $(BiO)_2CO_3$ (Fig. 4a) sample consists of many flower-like hierarchical microspheres self-assembled by nanosheets. The as-prepared microspheres have an average diameter of 0.8~0.9 μm (Fig. 4a) and thickness of 0.6~0.8 μm (Fig. 4b). Fig. 4a also reflects that the concavity with an average diameter about 0.4 μm in the center is actually hollow. The micro hollow architectures are further demonstrated in Fig. 4c. The HRTEM image of a single nanoplate on the edge of the microsphere is demonstrated in Fig. 4d. A clear lattice spacing of 0.272 nm well assigned to the (110) crystal plane of $(BiO)_2CO_3$, indicating the preferential growth of $(BiO)_2CO_3$ nanoplates along certain axis.

Fig. 5a apparently reflects that the flower-like hierarchical microspheres partially collapsed and transformed into stacked nanosheets as a result of Bi particles generation. The self-assembled nanosheets of BOC-WE also become smaller and less regular in comparation with that of pure BOC (Fig. 5a and Fig. 5b). The enlarged view of TEM (Fig. 5c) demonstrated that the hollow architecture was not changed when some partial $(BiO)_2CO_3$ was reduced to Bi elements. Fig. 5d reflects the typical HRTEM image of BOC-WE, which is taken on the edge of a single nanosheet. Except for the observation of the lattice spacing (0.272 nm) of (110) crystal plane in $(BiO)_2CO_3$, the lattice spacing (0.280 nm) corresponding to (012) lattice plane of Bi particles could also be detected (Fig. 5d and enlarge view in Fig. S1), which is in consistent with the XRD result.

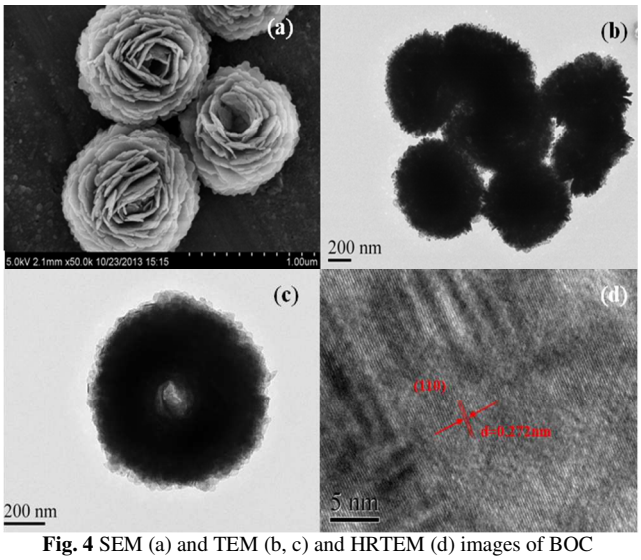

Fig. 4 SEM (a) and TEM (b, c) and HRTEM (d) images of BOC

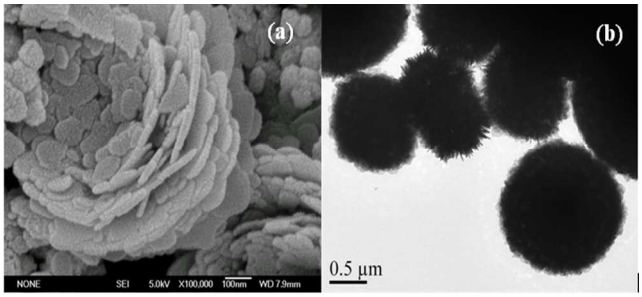

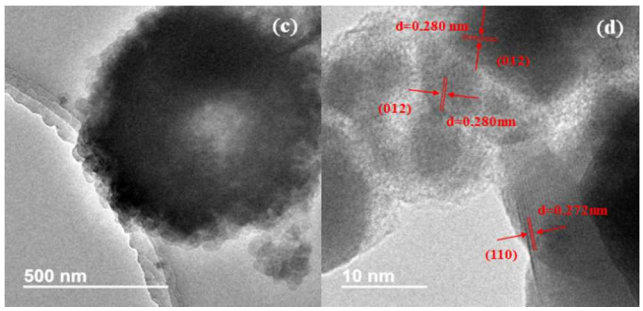

Fig. 5 SEM (a) and TEM (b, c) and HRTEM (d) images of BOC-WE.

3.4. BET surface areas and pore structure

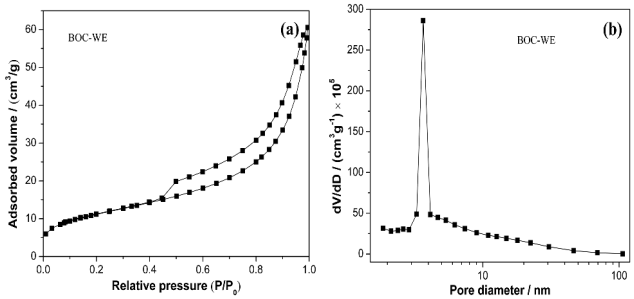

Fig. 6 N_2 adsorption-desorption isotherms (a) and pore-size distribution curves (b) for BOC-WE sample.

The nitrogen adsorption-desorption isotherms and corresponding pore size distribution curves of the BOC-WE sample are displayed in Fig. 6. According to the Brunauer-Deming-Deming-Teller (BDDT) classification, the majority of physisorption isotherms is close to type IV (Fig. 6a), which reflects the presence of mesopores in BOC-WE. This result is also demonstrated by the pore-size distribution curves. Moreover, the shape of the hysteresis loops is of type H_3, suggesting the existence of slit-like pores.[21] This result is in agreement with the SEM observation. Fig. 6b depicted the corresponding pore size distribution curves of the samples. The pore-size distribution range for the samples is broad in the range of 2 to 70 nm and unimodal with some small mesopores (3.6 nm), confirming the formation of mesopores.[44] The mesopores can be attributed to the pores formed among the aggregated nanosheets. The BET surface areas and the pore volume of BOC-WE are measured to be 40 m^2g^{-1} and 0.093 cm^3g^{-1}, smaller than that of pure BOC 46 m^2g^{-1} and 0.12 cm^3g^{-1},[39] which is ascribed to the partial collapse of flower-like hierarchical microspheres, consistent with the SEM results. Generally, porous architectures are in favour of the photocatalytic process by providing efficient transport pathways for reactants and products and facilitating the adsorption of pollutants for degradation.[21] Nevertheless, considering the subsequent results of photocatalytic experiments, we can see that the BET and porous volume do not play a crucial factor for enhancing the photocatalytic performance of the BOC-WE systems.

Table 1 The S_{BET}, pore volume, peak diameter, NO removal ratio and NO_2 fraction of BOC and BOC-WE samples as well as that of the reference samples from literature.

Sample name	S_{BET} (m^2/g)	Pore volume (cm^3/g)	Peak diameter (nm)	NO η (%)	NO_2 fraction (%)

BOC[33]	46	0.12	2.0/10.1	19.1	27.3
BOC-WE	40	0.093	1.7/3.8	37.2	13.6
BiOI[5]	6	0.027	3.7/18.3	14.9	—
BiOBr[43]	11	0.023	—	21.3	—
C-TiO_2[44]	123	—	—	21.8	—
C_3N_4[44]	13	0.087	3.6/30.0	25.5	36.6

3.5. Light absorption and charge separation

UV-Vis DRS spectroscopy study was also carried out in order to understand the optical properties of the BOC-WE and pure $(BiO)_2CO_3$. As shown in Fig. 7a, the pure BOC exhibits stronger absorption in the UV region, which can be attributed to its more regular morphology than the collapsed microspheres of BOC-WE. Because the special 3D hierarchical structure could generate multiple light scattering and reflecting effects, thus greatly strengthening the effective optical path-length of a photon and absorption probability.[33] In the visible light region, the light absorption is enhanced via deposition of the Bi on the surface of BOC. Moreover, a week absorption peak cantered at 550 nm is observed, which could be due to the SPR property of metallic Bi. As demonstrated, several previous documents reported that as a non-noble metal, Bi displays SPR property in the near ultraviolet and visible light range.[45] The bathochromic effect of the SPR peak is observed compared with the pure Bi (50 to 100 nm), which can be assigned to the different sizes of Bi particles.[45] The SPR absorption of Bi (10~70 nm in size) was observed at around 550 nm assigned to the SPR effect and light scattering, as reported by Wang et al.[28] Broad visible absorption band observed at about 450~600 nm of Bi-based composites photocatalysts was also observed.[30,31] The SPR absorption intensity of the BOC-WE seemed to be quite weak, because only a small amount of metallic Bi particles are deposited on the surface of BOC-WE.[33] Generally, the existence of semi-metallic Bi on the surface of $(BiO)_2CO_3$ microspheres can conspicuously strengthen the visible-light absorption through the surface plasmon resonance effect.

The recombination of charge carriers was investigated by Photoluminescence (PL) emission spectra. Fig. 7b reflects the room temperature PL spectra of the BOC-WE and pure BOC samples with an excitation wavelength of 280 nm. It can be seen that the fluorescence emission peaks are mainly centered at 350-425 nm, which contains both the UV and visible light regions. In general, a low PL intensity is generally indicative of high separation efficiency of electron–hole pairs.[33] The BOC-WE samples show apparently diminished PL intensity compared with pure BOC, which suggests that the deposition of Bi results in an obvious decline in the recombination rate of electron–hole pairs. This result is supported by the fact that the deposited Bi nanoparticles can act as electron traps increasing electron–hole separation.[30] In one word, the presence of metal Bi nanoparticles plays a crucial role in separating electron–hole pairs.

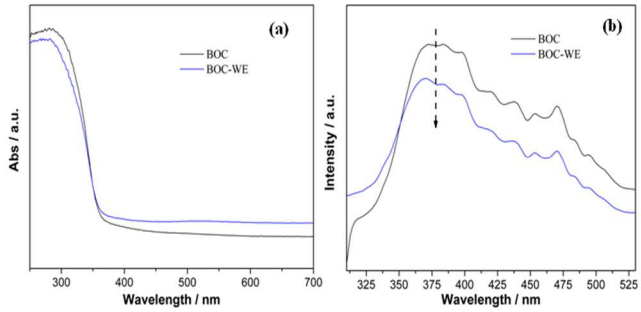

Fig. 7 UV-vis DRS (a) and PL (b) of BOC and BOC-WE.

3.6 Photocatalytic activity, enhancement mechanism and photochemical stability

NOx in low concentration of ppb level are representative indoor and outdoor air pollutants. The as-prepared BOC-WE samples were employed in the photocatalytic removal of NO in air to investigate their potential capability for air pollutant degradation a continuous reactor. Previous reports have demonstrated that NO is very stable and cannot be photolyzed under light irradiation without photocatalysts.[27] In the presence of photocatalytic materials, NO can react with photo-generated reactive radicals to produce HNO_3 as the final product.[21,27] Fig. 8a depicts the variation of NO concentration (C/C_0%) with irradiation time over BOC-WE samples under visible light irradiation with pure $(BiO)_2CO_3$ as references. As shown in Fig. 8a, the NO concentration for BOC-WE and BOC samples decrease rapidly due to the photocatalysis effect in the first 5-10 minutes. Nevertheless, several minutes later, the photocatalytic performance will be slightly decreased, which is ascribed to the generated reaction intermediates and final products occupying the active sites of photocatalysts during irradiation. The decent visible light photocatalytic activity of $(BiO)_2CO_3$ microspheres can be ascribed to the surface reflecting and scattering effect owing to the hierarchical architecture.[21] Significantly, the photocatalytic capability of the BOC-WE photocatalysts can reach to 37.2% after 30 min irradiation after equilibrium is reached, far more higher than that of pure $(BiO)_2CO_3$ (19.1%), as well as that of other types of visible light photocatalysts, C-doped TiO_2 (21.8%),[44] BiOBr (21.3%),[43] BiOI (14.9%)[5] and C_3N_4 (25.5%)[44] under the same test conditions.

Considering the similar morphology, surface areas and pore structure (Table 1) of pure $(BiO)_2CO_3$ and BOC-WE samples, we can draw a conclusion that the metallic Bi can act as an excellent cocatalyst for boosting the visible-light photocatalytic performance of BOC.[33] Hence, depositing metallic Bi, a superior non-noble metal-based cocatalyst onto the $(BiO)_2CO_3$ surface is an effective strategy to enhance the activity of $(BiO)_2CO_3$. As is well-known, NO_2 is an intermediate during the photocatalytic oxidation of NO. As an ideal photocatalyst for practical applications, the generation of NO_2 should be hindered. Fig. 8b shows the concentration variations of reaction intermediate of NO_2 monitored online during photocatalytic oxidation of NO. The fraction of NO_2 produced during photocatalytic reactions decreased from about 25% for BOC to almost 13% for BOC-WE, demonstrating the increasing photocatalytic oxidation ability. The more hydroxyl radicals (•OH) produced on BOC-WE can advance the oxidation of intermediate NO_2 to final NO_3^- in comparison with that of BOC (evidenced below by ESR spectra).[39] The final oxidation products of nitric acid or nitrate ions can be easily washed away by water wash.

The factors that propels the Bi cocatalyst-deposited $(BiO)_2CO_3$ microspheres with conspicuously enhanced visible-light performance and oxidation capability were further investigated. As previous reports shown, the enhancement in photocatalytic capability can be assigned to the synergetic effects of many factors, such as hierarchical structure, surface area, interfacial charge transfer and efficient separation of photo-induced electron-hole pairs.[21,33]

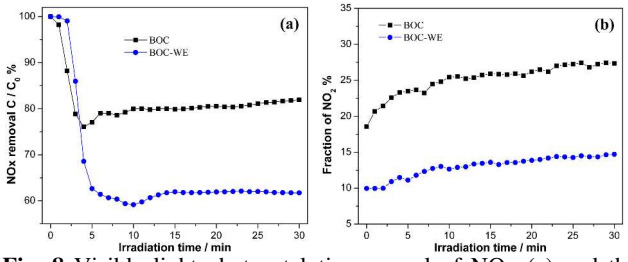

Fig. 8 Visible light photocatalytic removal of NOx (a) and the fraction of intermediate NO_2 in gas phase (b).

Based on the above characterizations, the mechanism for enhanced photocatalytic performance of BOC-WE is illustrated in Fig. 9, which can be summarized to the synergetic effects of the following factors. Firstly, the SPR effect of spatially confined electrons in the deposited Bi nanoparticles favors the visible-light absorption of BOC-WE samples, as observed by UV-vis DRS analysis (Fig. 7a). Secondly, owing to the SPR effect, the Bi nanoparticles can be photoexcited, hence strengthening the surface electron excitation and interfacial electron transfer (Eq. (1)).[33,46] Thirdly, given that the Fermi level of metallic Bi (–0.17 eV) is higher than the conduction band of $(BiO)_2CO_3$ (0.20 eV), the photo-generated electrons would transfer from Bi particles to $(BiO)_2CO_3$ (Eq. (3)).[33] Upon the released electrons, Bi would shift to more positive potentials to produce positive charges. And similar to Ag cocatalyst in photocatalysis, Bi would return to its primordial state by accepting electrons from the valence band of $(BiO)_2CO_3$.[33,47] Thus, such interface transfer (I) of electrons from $(BiO)_2CO_3$ to Bi nanoparticles retards the recombination of electron–hole pairs in $(BiO)_2CO_3$.

Moreover, the SPR-mediated local electromagnetic field of Bi (II) also radioatively propels to the separation of electron–hole pairs in $(BiO)_2CO_3$.[33,48] Afterwards, these two types of photo-induced charge carriers would be transformed into active species (•OH) that are responsible for the degradation of pollutants (Eq. (4-6)). According to the fact that the redox potential of $O_2/•O_2^-$ is –0.33 eV, more negative than that of the CB of $(BiO)_2CO_3$ (0.20 eV), the CB electrons could not reduce the O_2 to superoxide radicals ($•O_2^-$) (Eq. (7)). Nevertheless, the self-generated photo-induced electrons of $(BiO)_2CO_3$ (Eq. (2)) due to the light scattering effects, accompanied with the electrons transferred from Bi, possess efficient potential to reduce O_2 to H_2O_2 (Eq. (4)) on account of the fact that the redox potential of O_2/H_2O_2 is 0.695 eV. Consequently, the generated H_2O_2 would be further transformed into •OH by capturing electrons.[49] Besides, the photo-generated holes can also oxidize OH^- into •OH radicals because the potential of the holes at the VB of $(BiO)_2CO_3$ (3.53 eV) is more positive than the redox potential of $OH^-/•OH$ (1.99 eV). Note that •OH radicals are major reactive oxidation species, which could adequately oxidize NO to for the final HNO_2 and HNO_3 products (Eqs. (8-9)).

The •OH radicals are further detected by DMPO-ESR spin-trapping, as depicted in Fig. 10. Four strong characteristic peaks with intensity ration of 1:2:2:1 were clearly observed for pure BOC and BOC-WE samples, which testified that the massive production of •OH radicals. Further observation in Fig. 10 suggests that the signal of BOC-WE is much stronger than that of

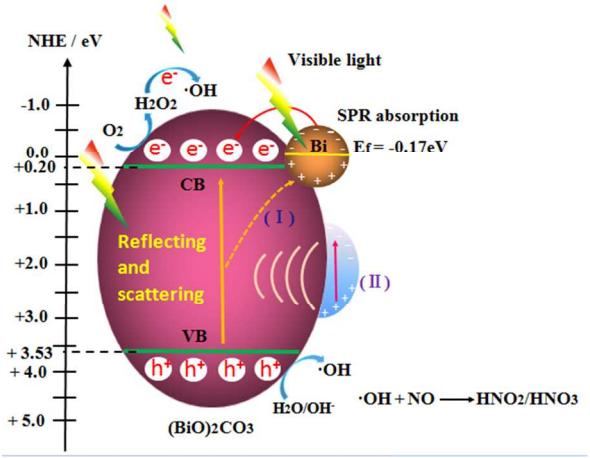

Fig. 9 Illustration of visible-light photocatalysis mechanism of BOC-WE for NOx oxidation. Interface transfer of electrons from $(BiO)_2CO_3$ to Bi (I), and local electromagnetic field of Bi (II).

$$Bi + h\nu \longrightarrow e^-(Bi) \quad (1)$$

$$BOC + h\nu \longrightarrow e^-(BOC) + h^+(BOC) \quad (2)$$

$$e^-(Bi) \longrightarrow e^-(BOC) \quad (3)$$

$$2e^-(BOC) + O_2 + 2H^+ \longrightarrow H_2O_2 \quad (4)$$

$$H_2O_2 \longrightarrow 2•OH \quad (5)$$

$$h^+(BOC) + H_2O \longrightarrow •OH(BOC) + H^+ \quad (6)$$

$$e^- + O_2 \not\rightarrow •O_2^- \quad (7)$$

$$2•OH + NO \rightarrow NO_2 + H_2O \quad (8)$$

$$NO_2 + •OH \rightarrow NO_3^- + H^+ \quad (9)$$

pure BOC under visible-light irradiation. This result reflects that BOC-WE samples could produce more radicals, which is pivotal for enhancing photocatalytic performance and oxidation capability. The production of more •OH radicals by BOC-WE is ascribed to the co-contribution of SPR effect of Bi particles and transfer of electron from Bi particle to BOC.[33] In conclusion, similar to the noble metals (Ag and Au), the metallic Bi particles exhibit a special noble metal-like behaviour in consideration of the contributions for enhancing visible-light absorption and accelerating charge separation and transfer because of the SPR effect. Thus, the SPR effect of Bi could conspicuously promote the visible light photocatalytic activity. As Bi element is much cheaper than that of noble metals, Bi can be a potential substitute for noble metals in enhancing photocatalysis through SPR.

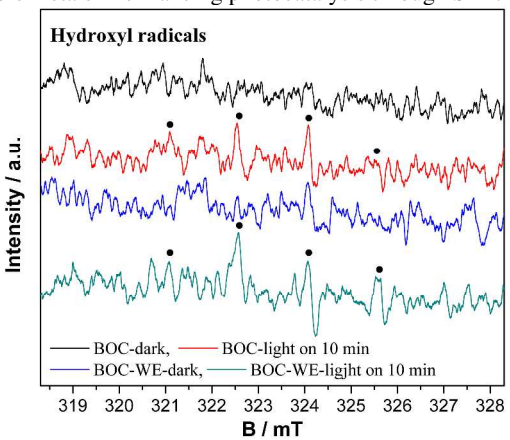

Fig. 10 DMPO-ESR spinning trapping for detection of hydroxyl radicals under visible light irradiation.

In consideration of practical applications, an ideal photocatalyst should possess photochemical stability and durability under repeated irradiation.[33] The repeated visible light photocatalytic capability of BOC-WE is depicted in Fig. 11a. No distinct activity decay is observed after continuous 600 min irradiation, which demonstrates that the BOC-WE composite is stable and cannot be easily photo-corroded during the photocatalytic process. Furthermore, the stability of BOC-WE is further confirmed with the TEM image of BOC-WE after long term photocatalytic test, which is almost identical to fresh samples (Fig. 11b). These results imply that the Bi-deposited $(BiO)_2CO_3$ have excellent stability in structure and activity.

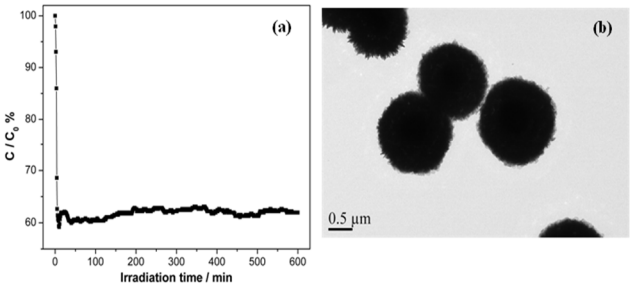

Fig. 11 Visible light photocatalytic removal of NOx with long term irradiation (a) and TEM image of the BOC-WE after long term visible-light photocatalytic test (b).

4. Conclusion

In summary, one-pot solvent-controlled synthesis strategy was firstly developed to in-situ deposit Bi cocatalyst on $(BiO)_2CO_3$ microspheres. In this solvent-controlled process, ethylene glycol functioned as a reductant and could reduce Bi^{3+} to metallic Bi. The introduction of Bi particles has a pivotal effect on the morphology, optical and electronic properties, of $(BiO)_2CO_3$. The Bi-cocatalyst deposited $(BiO)_2CO_3$ microspheres demonstrated conspicuously improved photocatalytic capability and oxidation ability for NOx purification, compared with that of individual $(BiO)_2CO_3$. The catalytic behavior of Bi nanoparticles acts as a cocatalyst is similar to that of noble metals. The enhanced visible-light photocatalytic activity of BOC-WE can be ascribed to the synergistic effects of SPR effect, increased visible light absorption and efficient separation of electron–hole pairs induced by Bi nanoparticles. In addition, DMPO-ESR results demonstrated that the hydroxyl radicals were confirmed to be the main active species for NO photo-oxidation. The BOC-WE could produce more hydroxyl radicals than that of BOC, which was responsible for the enhanced photo-oxidation ability. Ideally, the as-prepared BOC-WE also exhibited excellent photochemical stability in the aspects of activity and microstructure. The present work has demonstrated the high feasibility for the utilization of low cost Bi nanoparticles as a substitute for noble metals to improve performance of other photocatalytic materials. This work could not only provide new insights into the in situ fabrication of metal/semiconductor nanocomposites, but also paves a way for the modification of photocatalysts with non-noble metals as cocatalyst to achieve high-performance photocatalysts for practical applications.

Acknowledgement

This research is financially supported by the National Natural Science Foundation of China (51478070, 51108487), and the Natural Science Foundation of Chongqing (cstc2013jcyjA20018).

*To whom correspondence should be addressed.

Phone/Fax: +86-23-62769785-605. E-mail: syhsyj@163.com (Yanjuan Sun), andyzhangwei@163.com (Wei Zhang).

Reference

1 C. Su, X. Ran, J. Hu, and C. Shao, *Environ. Sci. Technol.*, 2013, **47**, 11562.
2 F. Dong, Z.Y. Wang, Y.H. Li, W.K. Ho and S.C. Lee, *Environ. Sci. Technol.*, 2014, **48**, 10345.
3 P. Wang, B.B. Huang, Y. Dai and M.H. Whangbo, *Phys. Chem. Chem. Phys.*, 2012, **14**, 9813.
4 S.G. Kumar and K.S.R. Koteswara Rao, *RSC Adv.*, 2015, **5**, 3306.
5 F. Dong, Y.J. Sun, M. Fu, W.K. Ho, S.C. Lee and Z.B. Wu, *Langmuir*, 2012, **28**, 766.
6 F. Dong, Z.W. Zhao, T. Xiong, Z.L. Ni, W.D. Zhang, Y.J. Sun and W.K. Ho, *ACS Appl. Mater. Interfaces*, 2013, **5**, 11392.
7 Z.W. Zhao, Y.j. Sun and F. Dong, *Nanoscale,* 2015, **7**, 15.
8 H.W. Huang, K. Liu, K. Chen, Y.L. Zhang, Y.H. Zhang and S.C. Wang, *J. Phys. Chem. C*, 2014, **118**, 14379.
9 A. Bumajdad and M. Madkour, *Phys. Chem. Chem. Phys.*, 2014, **16**, 7146.
10 J.X. Low, S.W. Cao, J.G. Yu and S. Wageh, *Chem. Commun.*, 2014, **50**, 10768.
11 C. Han, M.Q. Yang, B. Weng and Y.J. Xu, *Phys. Chem. Chem. Phys.*, 2014, **16**, 16891.
12 L.W. Zhang and Y. F. Zhu, *Catal. Sci. Technol.*, 2012, **2**, 694.
13 J. Li, Y. Yu and L. Z. Zhang, *Nanoscale*, 2014, **6**, 8473.
14 S. M. Sun and W. Z. Wang. *RSC Adv.*, 2014, **4**, 47136.
15 N. Zhang, R. Ciriminna, M. Pagliaro and Y. J. Xu, *Chem. Soc. Rev.*, 2014, **43**, 5276.
16 H.W. Huang, S.B. Wang, N. Tian, Y. H. Zhang, *RSC Adv.*, 2014, **4**, 5561.
17 Y.S. Xu and W.D. Zhang, *Appl. Catal. B.*, 2013, **140-141**, 306.
18 R. Chen, M. H. So, J. Yang, F. Deng, C. M. Che and H. Z. Sun, *Chem. Commun.,* 2006, **42**, 2265.
19 G. Cheng, H. M. Yang, K. F. Rong, Z. Lu, X. L. Yu and R. Chen, *J. Solid State Chem.,* 2010, **183**, 1878.
20 S. J. Peng, L. L. Li, H. T. Tan, Y. Z. Wu, R. Cai, H. Yu, X. Huang, P. N. Zhu, S. Ramakrishna, M. Srinivasan and Q. Y. Yan, *J. Mater. Chem. A,* 2013, **1**, 7630.
21 F. Dong, Q.Y. Li, Y. Zhou, Y.J. Sun, H.D. Zhang and Z.B. Wu, *Dalton Trans.*, 2014,**43**, 9468.
22 P. Madhusudan, J. R. Ran, J. Zhang, J. G. Yu and G. Liu, *Appl. Catal. B.,* 2011, **110**, 286.
23 P.Madhusudan, J. G. Yu, W. G. Wang, B. Cheng and G. Liu, *Dalton. Trans.,* 2012, **41**, 14345.
24 X.C. Zhang, T.Y. Guo, X.W. Wang, Y.W. Wang, C.M. Fan, H. Zhang, *Appl. Catal. B.*, 2014, **150–151**,486.
25 F. Dong, X. Feng, Y.X. Zhang, C.F. Gao and Z.B. Wu, *RSC Adv.*, 2015, **5**, 11714-11723.
26 F. Dong, T. Xiong, Y.J. Sun, Z.W. Zhao, Y. Zhou, X. Feng and Z. B. Wu, *Chem. Commun.*, 2014, **50**, 10386.
27 Q. Zhang,Y. Zhou, F. Wang, F. Dong, W. Li, H.M. Li and Greta R. Patzke, J. Mater. Chem. A., 2014, **2**, 11065.
28 Z. Wang, C.L. Jiang, R. Huang, H. Peng and X.D. Tang, *J. Phys. Chem. C*., 2014, **118**, 1155.
29 X.W. Liu, H.Q. Cao and J.F. Yin, *Nano Res.*, 2011, **4**, 470.
30 S. X. Weng,; B.B. Chen, L.Y. Xie, Z.Y. Zheng and P. Liu, *J. Mater. Chem. A,* 2013, **1**, 3068.
31 Y. Yu, C.Y. Cao, H. Liu, P. Li, F.F. Wei, Y. Jiang and W. G. Song, *J. Mater. Chem. A,* 2014, **2**, 1677.
32 C. Chang, L.Y. Zhu, Y. Fu and X.L. Chu, *Chem. Eng. J.,* 2013, **233**, 305.
33 F. Dong, Q.Y. Li, Y.J. Sun and W.K. Ho, *ACS Catal.,* 2014, **4**,4341.
34 F. Dong, A. Zheng, Y.J. Sun, M. Fu, B.Q. Jiang, W.K. Ho, S. C. Lee and Z.B. Wu, *CrystEngComm*, 2012, **14**, 3534.
35 C. Z. Wu and Y. Xie, *Chem. Commun.,* 2009, 5943-5957.
36 P. Madhusudan, J. Zhang, B. Cheng and G. Liu, *CrystEngComm*, 2013,**15**, 231.

37 Y.N. Wang, K.J. Deng and L.Z. Zhang, *J. Phys. Chem. C*, 2011, **115**,14300.
38 K. Gurunathan, *Int. J. Hydrogen Energ*., 2004, **29**, 933.
39 Z.H. Ai, W.K. Ho, S.C. Lee and L.Z. Zhang, *Environ. Sci. Technol.,* 2009, **43**, 4143.
40 R. Nyholm, A. Berndtsson and N. Martensson, *J. Phys. C*: *Solid St. Phys.*, 1980, **13**, L1091.
41 S. Shamaila, A K.L. Sajjad, F. Chen and J.L. Zhang, *Appl. Catal., B*., 2010, **94**, 272.
42 F. Dong, H.T. Liu, W.K. Ho, M. Fu and Z.B. Wu, *Chem. Eng. J*., 2013, **214**, 198.
43 W.D. Zhang, Q. Zhang and F. Dong, *Ind. Eng. Chem. Res*., 2013, **52**, 6740.
44 F. Dong, Y.H. Li, W.K. Ho, H.D. Zhang, M. Fu and Z.B. Wu, *Chin. Sci. Bull*., 2014, **59**, 688.
45 J. Toudert, R. Serna, M. J. Castro, *J. Phys. Chem. C,* 2012, **116**, 20530.
46 J. Ren, W. Z. Wang, S. M. Sun, L. Zhang and J. Chang, *Appl. Catal., B*., 2009,**92**,50.
47 H. Cheng, B. Huang, P. Wang, Z. Wang, Z. Lou, J. Wang, X. Qin, X. Zhang and Y. Dai, *Chem. Commun.,* 2011, **47**, 7054.
48 H. A. Atwater and A. Polman, *Nat. Mater.*, 2010, **9**, 205.
49 Q. J. Xiang, J. G. Yu, B. Cheng and H. C. Ong, *Chem. Asian. J.,* 2010, **5**, 1466.